Journal of Science and Technology in Civil Engineering, HUCE, 2026, 20 (3): 31–50

A SEQUENTIAL COMPUTATIONAL FRAMEWORK FOR RECYCLED-MATERIAL 3D PRINTING CONCRETE: FROM PUMPING FLOW TO BUILDABILITY LIMIT

Ta Minh Phuong Bao[a,*], Luc Courard[a]

[a]*Department Architecture, Geology, Environment & Constructions, Faculty of Applied Sciences, University of Liège, Quartier Polytech 1, Allée de la Découverte 9, 4000 Liège, Belgium*

Article history:
Received 19/8/2026, Revised 21/9/2026, Accepted 23/9/2026, Available online 25/9/2026, Version of Record 25/9/2026

Abstract

Recycled sand is increasingly used as a sustainable substitute for natural fine aggregate in 3D printing concrete (3DPC), yet the ultra-fine fraction generated during recycling, recycled concrete crushed fine (RCCF, < 63 μm), remains underexploited as a partial cement substitute. Existing studies on this material are limited to experimental characterisation, without extending to computational prediction of behaviour throughout the printing process. This study addresses that gap by developing a sequential Computational Fluid Dynamics (CFD) and Finite Element Method (FEM) framework to evaluate an optimised mortar mix incorporating recycled sand and 10% RCCF (mix FIN 10). The fresh-state flow within the pumping pipe was simulated in OpenFOAM using a Bingham model and validated against nine physical printing trials, with an average deviation of 22% in volumetric flow rate. The post-extrusion structural response was then simulated in CalculiX using a layer-wise activation scheme and a Mohr–Coulomb plasticity model calibrated from fresh-state compression and direct shear tests. The simulation showed that the printed wall could be successfully built up to a height of 540 mm (36 layers) without collapse, reaching a numerically predicted buildability limit of 555 mm at layer 37. The results demonstrate the feasibility of RCCF as a cement substitute and establish an experimentally calibrated, process-scale computational methodology linking pumping flow to post-deposition structural stability for this recycled-material 3DPC mix.

Keywords: 3D printing concrete; recycled concrete crushed fine; fresh-state properties; yield stress; viscosity; CFD modelling; FEM modelling; buildability.

1. Introduction

Three-dimensional printing concrete has attracted growing interest as an automated, formwork-free construction method capable of optimising structural geometry, thereby substantially reducing material consumption, construction time, and labour requirements compared with conventional methods [1]. Within this context, 3DPC has also been assessed for its potential alignment with the circular economy framework, where the technology has been shown to offer clear benefits across all three pillars of the waste hierarchy: reduce, reuse, and recycle [2].

At the same time, the construction industry generates a substantial and continuously growing volume of construction and demolition (C&D) waste, estimated globally at over 2 billion tonnes annually, of which concrete and sand-based materials account for the largest share [3, 4]. Incorporating recycled and waste-derived materials, including recycled sand and concrete fines, crushed glass, fly ash, crumb rubber, and recycled plastics, into 3D-printable mixes has therefore emerged as an important strategy

*Corresponding author. *E-mail address:* mpbta@uliege.be (Bao, T. M. P.)
https://doi.org/10.31814/stce.huce2026-20(3)-02 p-ISSN 1859-2996; e-ISSN 2734-9268
© 2026 The Author(s). Published by Hanoi University of Civil Engineering. Licensed under CC BY-NC-ND 4.0.

for improving the sustainability of the technology, simultaneously reducing natural sand extraction and limiting landfill waste [5, 6]. This trend is consistent with broader efforts within the region to valorise construction waste as structural material, including the pelletisation of waste concrete fines into synthetic aggregate [7] and the use of recycled aggregates in reinforced concrete columns [8], the partial replacement of fine aggregate with shell waste in concrete block production [9] and the reuse of crushed construction and demolition waste as reactive media in environmental remediation applications [10].

Building on this, numerous experimental studies have confirmed the feasibility of replacing natural sand with recycled sand in 3D-printable mortar, including at full (100%) replacement levels. Yuan et al. [11] showed that mortars incorporating recycled fine aggregate can still achieve satisfactory printability (extrudability and buildability), although compressive strength, flexural strength, and interlayer bond strength tend to decrease as the replacement ratio increases. Al Thib et al. [12] further proposed a dedicated mix-design methodology for 3D-printable mortar based entirely on recycled sand, validated through actual printing trials to confirm the feasibility of the resulting mixes.

Within the recycling process of sand and concrete, a fraction of ultra-fine particles is inevitably generated, referred to as recycled concrete crushed fine (RCCF, typically below 63 μm). Despite arising as an unavoidable by-product of aggregate recycling, this fraction remains considerably less explored than conventional recycled sand, as most existing studies have focused on coarser recycled fractions suitable for direct use as fine aggregate.

A closely related material, recycled concrete powder (RCP), has more recently attracted attention as a partial cement replacement in 3DPC mixes. Cavalcante et al. [13] investigated RCP obtained from two distinct sources as a 50% Portland cement replacement in printable pastes and mortars, reporting a substantial increase in both static and dynamic yield stress, together with reduced extrudability and buildability. Similarly, Qian et al. [14] demonstrated that recycled construction powder can be incorporated into 3D-printable mortar through particle-packing optimisation, improving early yield stress while requiring careful adjustment of cementitious content to preserve mechanical performance.

While these studies have established a valuable understanding of how RCP influences rheology, printability, and mechanical strength, they remain confined to experimental characterisation at the material level. None of them extends this understanding to computational prediction of material behaviour across the full printing process, from pumping through post-deposition structural response, leaving an important gap for materials incorporating RCCF specifically.

Beyond the material level, a printable mortar mix must also perform reliably across two critical stages of the 3DPC process. The first is the flow behaviour of the mortar within the pumping system and delivery pipe, prior to extrusion through the nozzle. The second is the structural response of the deposited material after extrusion, namely its ability to sustain the self-weight of subsequently printed layers without excessive deformation or collapse, commonly referred to as buildability.

To date, these two stages have largely been investigated through separate numerical approaches. On the flow side, CFD models based on Bingham or Herschel–Bulkley constitutive laws have been developed to predict extruded layer geometry and flow behaviour of cementitious materials [15]. On the structural side, a separate body of work has developed FEM and mechanistic models to predict post-deposition failure, distinguishing between elastic buckling and plastic collapse of printed walls [16–18].

While both modelling approaches have matured independently, studies sequentially linking flow-stage CFD simulation with post-deposition FEM structural analysis within a single, process-scale framework remain scarce. This gap is particularly pronounced for mixes incorporating recycled mate-

rials: existing buildability assessments of such mixes, for example the fine-recycled-aggregate mortar studied by De Vlieger et al. [19], remain based on experimental or simplified analytical indicators rather than a validated computational framework spanning both the pumping and post-deposition stages.

To address this gap, the present study develops a Sequential Computational Framework for Recycled-Material 3D Printing Concrete, capable of predicting the behaviour of an optimised mortar mix incorporating recycled sand and 10% RCCF as a partial cement substitute. The fresh-state flow of the mix within the delivery pipe is simulated in OpenFOAM using a Bingham model, validated against nine physical printing trials, while the post-extrusion structural behaviour is simulated in CalculiX using a layer-wise activation scheme, with material response governed by a Mohr–Coulomb plasticity model calibrated from fresh-state compression and direct shear tests on the same mix.

The objectives of this research are to: (i) demonstrate the printability of the mix through experimental verification, including extrudability and buildability; (ii) validate the sequential CFD-FEM framework against physical printing trials; and (iii) identify the buildability limit of the mix and characterise its governing failure mechanism. Through this approach, the study seeks to provide a validated computational pathway for predicting the printing performance of mortar mixes incorporating ultra-fine recycled construction waste in 3D printing concrete applications.

2. Materials and mix design

2.1. Materials

The mortar was prepared using CEM III A 52.5 N cement (Fig. 1(a)), chosen for its reduced carbon footprint due to partial clinker replacement by blast furnace slag.

Two fine aggregates were used: natural river sand (Fig. 1(b)) and recycled sand (Fig. 1(c)) sourced from construction and demolition waste. RCCF (particle size < 63 µm) was incorporated as a partial cement substitute, together with a polycarboxylate-based superplasticiser to maintain workability (shown in Fig. 1(d) and Fig. 1(e)).

The basic properties of the fine aggregates are summarised in Table 1, the particle size distribution of sand is shown in Fig. 2.



(a) Cement CEM III A 52.5



(b) Natural sand 0–2 mm



(c) Recycled sand (0–2 mm)



(d) Recycled crushed concrete fine 0–63 µm



(e) Superplasticiser Sika betonverflussiger BV 3M

Figure 1. Materials used in this study

Table 1. Basic properties of fine aggregates

Fine aggregate	Density (kg/m^3)	Maximum particle size (mm)	Water absorption (%)
Natural sand	2650	2	0.18
Recycled sand	2400	2	14.0

RCCF has a density of 2400 kg/m^3 and is primarily composed of quartz (> 60%), with calcite and feldspar-group minerals (albite, orthoclase) as secondary constituents; its full mineral composition is given in Table 2.

Table 2. Mineral composition of the RCCF

Mineral	Percentage (%)
Quartz – SiO_2	60.53%
Muscovite (2M1) – $KAl_2(AlSi_3O_{10})(OH)_2$	11.80%
Albite – $NaAlSi_3O_8$	8.47%
Orthoclase – $KAlSi_3O_8$	4.84%
Calcite – $CaCO_3$	9.34%
Chlorite IIb	5.02%

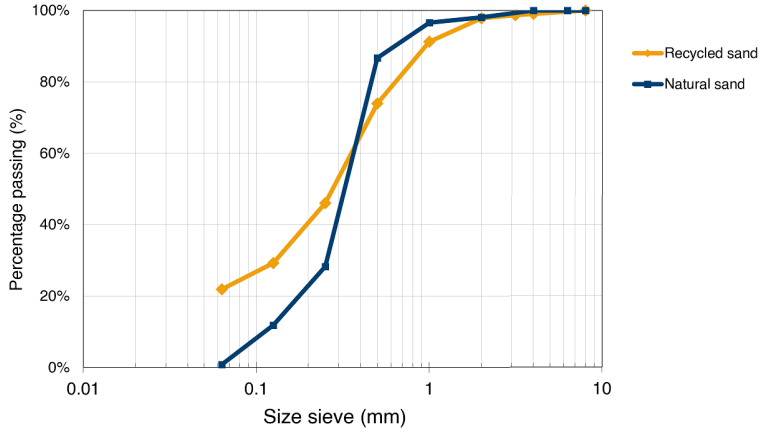


Figure 2. Particle size distribution of sand

2.2. *Mix composition*

The mix proportions were established based on a survey of water-to-binder ratios (W/B) and sand-to-binder ratios (S/B) commonly reported for 3D-printable cementitious materials, which typically fall within 0.30–0.40 and 1.0–1.5, respectively [20–24]. Within this range, a W/B of 0.40 and an S/B of 1.50 were adopted, as this combination consistently exhibited a Bingham-type rheological response with moderate yield stress and plastic viscosity, avoiding both the near-fluid behaviour associated with lower S/B ratios and the excessively stiff, poorly extrudable behaviour associated with lower W/B ratios. Natural sand was replaced with recycled sand at a fixed ratio of 25:75, the highest recycled content found to maintain adequate compressive strength, in line with sustainability considerations and consistent with high replacement levels reported in prior 3D-printable recycled sand mortars [11].

Owing to the substantially higher water absorption of recycled sand compared with natural sand, an additional amount of water equal to the absorption differential was added during mixing to com-

pensate for this effect, ensuring that the effective W/B ratio remained constant across the mix. However, the higher water absorption and rougher, more angular surface texture of recycled sand also tend to reduce the workability of the fresh mixture; a superplasticiser was therefore incorporated to counteract this loss of workability and maintain adequate flowability and extrudability for printing.

RCCF was subsequently incorporated at a 10% cement replacement level to evaluate its potential as a partial cement substitute. The corresponding mix proportions are given in Table 3.

Table 3. Mix proportions of FIN 10

Mixture	W/B	S/B	%NS	%RS	% Cement	%RCCF	Quantities (kg/m^3)						
							Cement	NS	RS	RCCF	Water	Added water	Superpl. (%wob)
FIN 10	0.40	1.50	25%	75%	90%	10%	672	280	840	75	299	116	1.51

NS: natural sand; RS: recycled sand; RCCF: recycled concrete crushed fine; W/B: water-to-binder ratio; S/B: sand-to-binder ratio; Superpl.: superplasticiser; wob: weight of binder. All proportions (%NS, %RS, % Cement, %RCCF) are expressed by weight.

3. Verification of printability

To evaluate the printability of mix FIN 10, a laboratory-scale 3D concrete printer was employed for trial printing, comprising a 3-axis gantry system coupled with a material pump. The mortar was mixed and fed into the pump, which delivered it through a delivery pipe with a diameter of 2.5 cm and a length of 3 m to the printer nozzle, following a pre-defined G-code path (Fig. 3). Printing was performed using a 34 mm diameter nozzle at a constant deposition speed of 75 mm/s, with a volumetric flow rate of approximately 3.9 L/min and an initial pump inlet pressure of 7 bar.

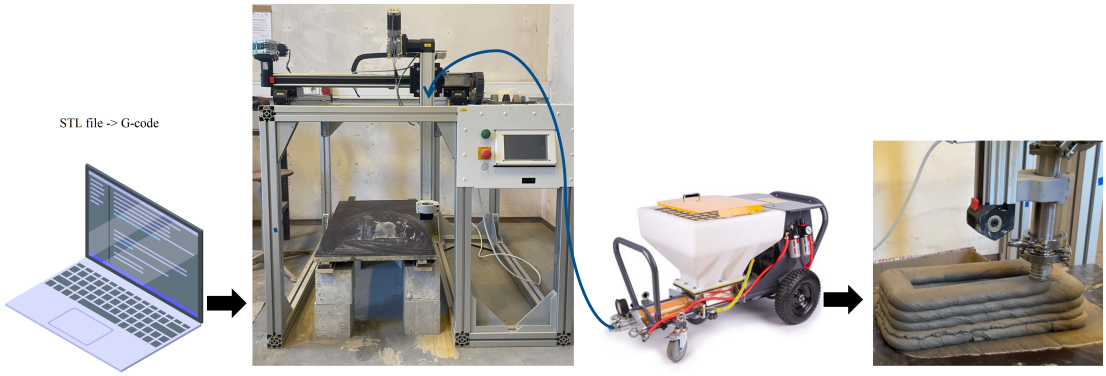


Figure 3. The 3D printing process: STL file converted to G-code, 3-axis gantry printer, material pump, and layer-by-layer deposition of the mortar

Each printed layer had a height of 15 mm and a width of 45 mm, with the nozzle-to-substrate distance kept equal to the layer height throughout printing. The test specimen was a hollow rectangular element with target dimensions of 150 mm (height) × 170 mm (width) × 350 mm (length).

The results of the printing trial are presented in Fig. 4. FIN 10 exhibited satisfactory pumpability, extrudability, and buildability throughout the trial printing process. Pumpability, governed mainly by the yield stress and viscosity of the mixture, was reflected in the consistent material deposition and the absence of pipeline clogging [25]. Extrudability, influenced by aggregate particle size, W/B ratio, and nozzle geometry [26], was confirmed by the continuous, smooth-surfaced filaments. Buildability, primarily governed by yield stress [27], was demonstrated by stable printing up to 10 layers without

deformation or collapse, this limit being imposed by the physical capacity of the printer rather than the mixture itself.

The maximum printed height reached approximately 150 mm, with no significant variation in layer width and no visible deformation or inclination between the second and final layers, indicating stable and consistent layer deposition and confirming that mix FIN 10 is extrudable, pumpable, and capable of satisfactory buildability up to the maximum height achievable by the printer.



(a) Angled view (b) Front view

Figure 4. Hollow rectangular specimen of mix FIN 10 printed with the actual 3D printer

4. Determination of material parameters for simulation

To enable predictive simulation of the printing process, two complementary sets of material parameters were characterised: rheological parameters (yield stress and viscosity) for the CFD simulation of pumping flow, and mechanical parameters (elastic modulus, cohesion, and internal friction angle), based on the Mohr–Coulomb failure criterion, for the FEM simulation of post-extrusion structural response.

4.1. Rheological parameters

Two key rheological parameters, yield stress and viscosity, were measured using a rheometer. The rheological behaviour of mortar is commonly described by the Bingham model, as shown in Eq. (1):

$$\tau = \tau_0 + \mu\dot{\gamma} \tag{1}$$

where τ_0 is the yield stress and μ is the plastic viscosity.

These two parameters were determined using a RheoCAD rotational rheometer, equipped with a four-blade system, from which yield stress and viscosity were directly calculated, as shown in Fig. 5.

To reflect the material state relevant to the printing process, the rheological parameters of mix FIN 10 were measured at 10 minutes after mixing, with each measurement repeated at least three times. The resulting yield stress and viscosity values are presented in Table 4.

Table 4. Rheological parameters of FIN 10

Mixture	Rheological equations	Rheological parameters	Yield stress SD (Pa)	Viscosity SD (Pa·s)
FIN 10	$y = 26.94x + 157.77$	yield stress = 157.77 Pa viscosity = 26.94 Pa·s	12	8

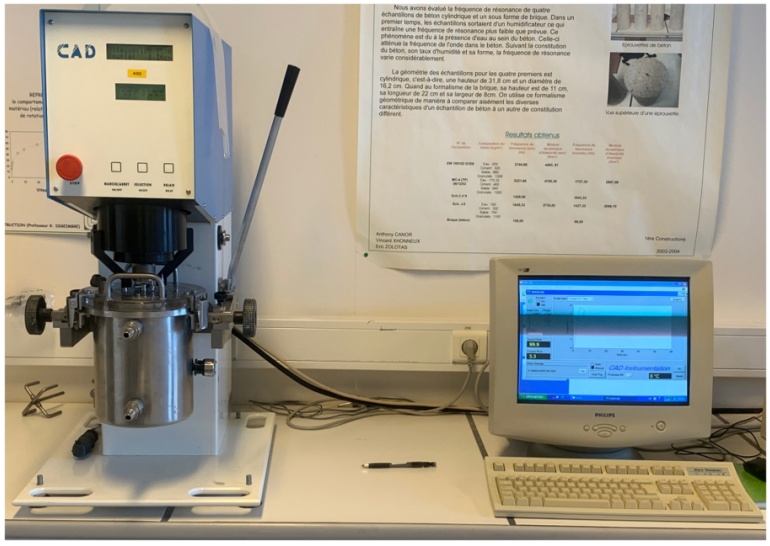
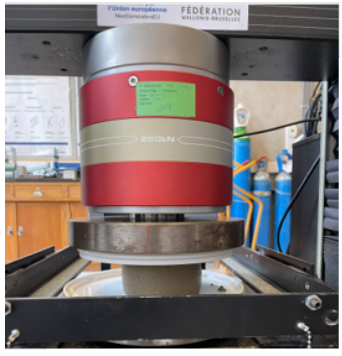


Figure 5. RheoCAD rotational rheometer used for the measurement of yield stress and viscosity

4.2. Mohr–Coulomb failure criterion

Four mechanical parameters governing the Mohr–Coulomb behaviour of mix FIN 10, namely Young's modulus (E), Poisson's ratio (ν), cohesion (c), and friction angle (φ), were determined experimentally at 10 minutes after mixing, matching the age relevant to printing. E and ν were obtained from unconfined uniaxial compression tests, following an approach adapted from the study by Wolfs et al. [28] for characterising fresh-state 3D-printed concrete, while c and φ were obtained from a direct shear test conducted in accordance with EN ISO 17892-10:2018. The equipment is shown in Fig. 6.



(a) Compression platen and specimen



(b) INSTRON compression testing machine



(c) Direct shear stress apparatus

Figure 6. Testing equipment used for the unconfined compression and direct shear tests

The dilation angle, ψ, governing the non-associated flow rule, was adopted from Wolfs et al. [28] as a widely used reference value for early-age 3D-printed concrete. The complete set of Mohr–Coulomb parameters used in the subsequent FEM simulation is summarised in Table 5.

The fresh-state density used in the CFD and FEM simulations (2167 kg/m^3) was obtained through direct measurement, by weighing and measuring the volume of actual fresh mortar specimens after mixing. This value therefore inherently reflects the true state of the mixed material, including the

effect of water absorption by the recycled sand during mixing. In contrast, the theoretical density calculated from the total mix constituent mass reported in Table 3 (approximately 2290 kg/m^3) assumes that all added water remains available as free water contributing to the design volume, without accounting for the portion absorbed into the internal pore structure of the recycled sand. This distinction explains the difference between the theoretical mix-design density and the experimentally measured fresh-state density adopted for the simulations.

Table 5. Mohr–Coulomb material parameters of mix FIN 10

Parameter	Value	Source
Young's modulus, E	135.05 kPa	Fresh unconfined compression test
Poisson's ratio, ν	0.29	Image-analysis of lateral strain
Density, ρ	2167 kg/m^3	Fresh-state mix density
Cohesion, c	6.50 kPa	Direct shear test
Friction angle, φ	41.3°	Direct shear test
Dilation angle, ψ	13°	Literature value from Wolfs et al. [28]

5. CFD simulation of pumping flow

5.1. Numerical setup

The fresh-state flow of mix FIN 10 within the delivery pipe was simulated in OpenFOAM, an open-source CFD platform previously applied to civil engineering flow problems such as wave propagation modelling [29]. The computational domain reproduced the actual pump-pipe-nozzle system, with a pipe length of 3 m and an internal diameter of 0.025 m (Fig. 7). Since 3D-printable mortar behaves as an incompressible, non-Newtonian fluid under laminar flow, the nonNewtonianIcoFoam solver was adopted, a modified version of the standard icoFoam solver extended to accommodate non-Newtonian constitutive models such as Herschel–Bulkley.

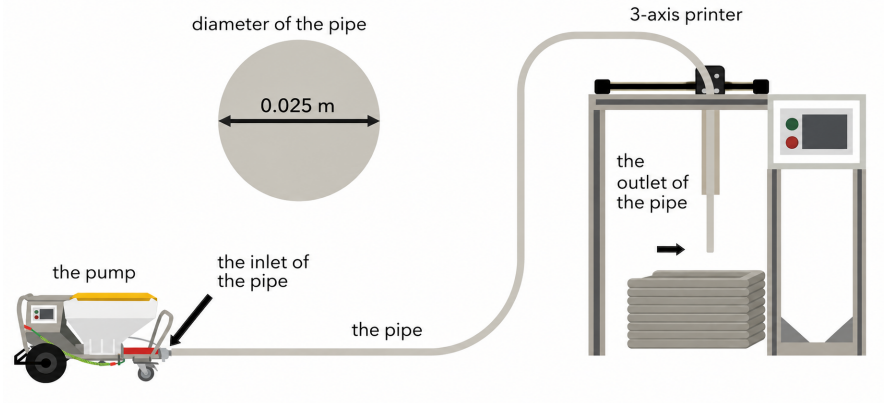


Figure 7. Geometry of the pumping pipe system, including the pump, pipe diameter, and printer nozzle outlet

nonNewtonianIcoFoam solves the pressure-velocity coupling through the PISO algorithm alone, rather than relying on outer corrector loops. Since it does not include an outer PIMPLE correction loop, the number of pressure-velocity correctors within the PISO loop was increased to 3 to compensate for the absence of outer iterations and to mitigate the risk of numerical divergence caused by sudden viscosity variations.

The mesh was generated in SALOME using an O-grid topology, which avoids the singularity that otherwise occurs at the axis of a circular domain and ensures stable, well-shaped elements. The

resulting mesh consisted of 292,281 nodes and 353,640 elements, including 280,000 hexahedral volume cells, with refined discretisation applied at the pipe inlet, outlet, and curved sections to ensure adequate resolution of the flow field (Fig. 8).

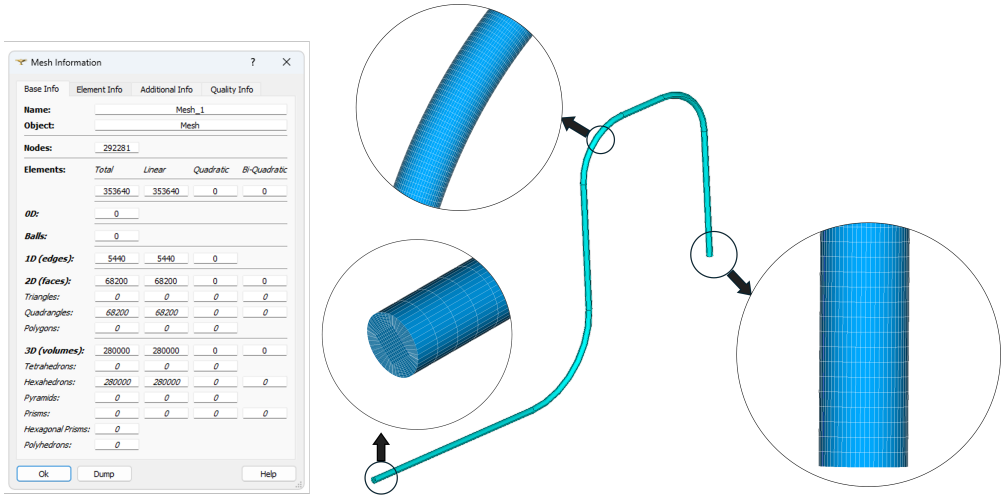


Figure 8. Mesh detail and mesh information of the pipe

The rheological behaviour of mix FIN 10 was described using the Herschel–Bulkley model, $\tau = \tau_0 + k\dot{\gamma}^n$, with the power-law index fixed at $n = 1$ to recover the Bingham response consistent with the rheometer-measured yield stress and viscosity. As OpenFOAM formulates the governing equations in kinematic form, all inputs had to be divided by the material density ($\rho = 2167$ kg/m^3) before being entered into the solver. The resulting parameters used in the simulation, including the inlet and outlet pressures derived respectively from the pump gauge pressure and the hydrostatic pressure at the nozzle outlet, are summarised in Table 6. A no-slip condition was imposed at the pipe wall, a zero-gradient condition at the outlet, and the flow was modelled as laminar, consistent with the low Reynolds number expected for a high-viscosity, high-yield-stress mortar.

Table 6. Simulation input parameters for mix FIN 10 (kinematic units)

Parameter	Value	Description
τ_0 (yield stress)	0.0728 m^2/s^2	Converted from 157.77 Pa
k (consistency index; equivalent to plastic viscosity for $n = 1$)	0.012 43 m^2/s	Converted from 26.94 Pa·s
ν_0 (limiting viscosity)	0.1243 m^2/s	Numerical regularisation at zero shear rate
n (power-law index)	1	Bingham model
p_{inlet}	276.94 m^2/s^2	Converted from 600,000 Pa (pump gauge pressure)
p_{outlet}	6.87 m^2/s^2	Converted from 14,880.79 Pa (hydrostatic pressure)

The pump inlet pressure was measured as an absolute reading of 7 bar. Since 100,000 Pa of this absolute reading corresponds to atmospheric pressure, the effective gauge pressure driving the flow through the pipe, i.e., the pressure value relevant to the CFD boundary condition, was 700,000 – 100,000 = 600,000 Pa. This gauge pressure was then converted to kinematic units by dividing by the mortar density, consistent with the pressure-based formulation of the solver used (nonNewtonianIco-

Foam), which solves for kinematic pressure (p/ρ) rather than absolute pressure.

It is noted that the parameter k listed in Table 6 is not identical to the coefficient k in Herschel–Bulkley model equation. OpenFOAM's Herschel–Bulkley implementation formulates the apparent viscosity directly in kinematic form, $\nu = \min\left(\nu_0, \tau_0/\dot{\gamma} + k\dot{\gamma}^{n-1}\right)$ [30], rather than in terms of shear stress as in Herschel–Bulkley equation. Consequently, k in Table 6 denotes a kinematic consistency index (m^2/s); for $n = 1$, $k = \mu/\rho$, obtained by dividing the measured plastic viscosity (26.94 Pa·s) by the mortar density.

5.2. Results

Under the prescribed pressure-driven boundary conditions, the simulated velocity field developed a stable, essentially uniform profile along the straight sections of the pipe, with no evidence of flow blockage, recirculation, or numerical instability at the converged mesh resolution (Fig. 9).

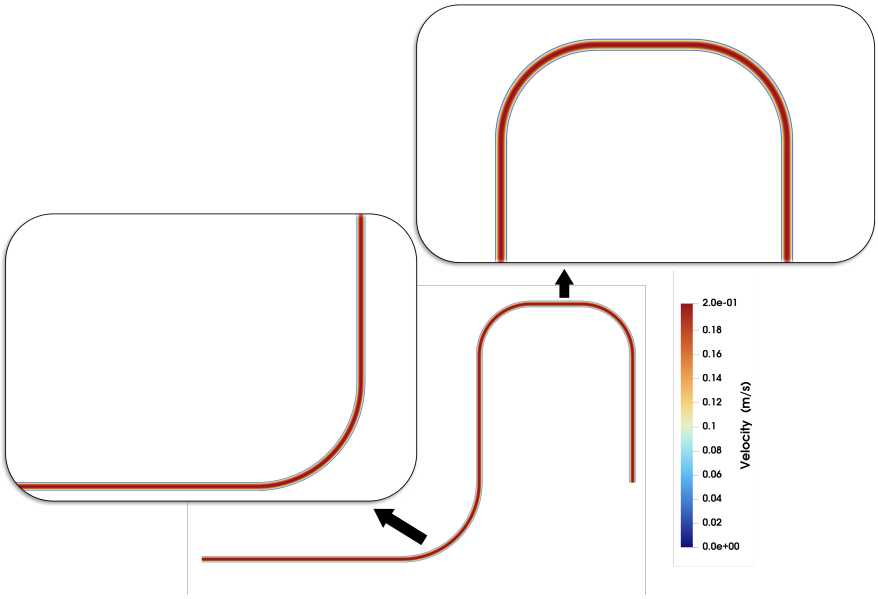


Figure 9. Simulated velocity profile of mix FIN 10 within the pumping pipe

The velocity remained consistent through the curved segments of the pipe, indicating that flow is governed primarily by the pressure differential between the inlet and outlet rather than by pipe geometry, consistent with the low Reynolds number regime typical of high-viscosity, high-yield-stress mortars. The maximum velocity, located at the pipe centerline, converged to approximately 0.20 m/s.

For a Bingham fluid, shear stress increases linearly from the centerline toward the wall; where this stress remains below the yield stress τ_0, the material translates as a rigid plug rather than deforming, while the outer annular region, where stress exceeds τ_0, shears and flows, with the highest shear stress, and therefore the highest risk of localised damage or segregation, occurring at the wall. This plug-flow behaviour, characteristic of high-yield-stress printable mortars, was used as the basis for interpreting the simulated velocity field.

Examining the velocity profile at the pipe outlet (Fig. 10) suggests the presence of a plug-flow zone, with a comparatively flat, near-uniform velocity region near the centerline; however, the profile remains stepped and not fully smooth at the current mesh resolution, so the plug boundary cannot be identified with full confidence from the raw OpenFOAM output alone. A preliminary mesh refinement

was tested, using two finer configurations of 403,200 and 630,000 cells; the maximum centreline velocity varied by less than 0.6% across all three meshes, indicating that the solution is effectively mesh-independent at the baseline resolution. A full mesh sensitivity analysis, including its effect on the resolution of the plug-flow boundary itself, is left for dedicated investigation in future work.

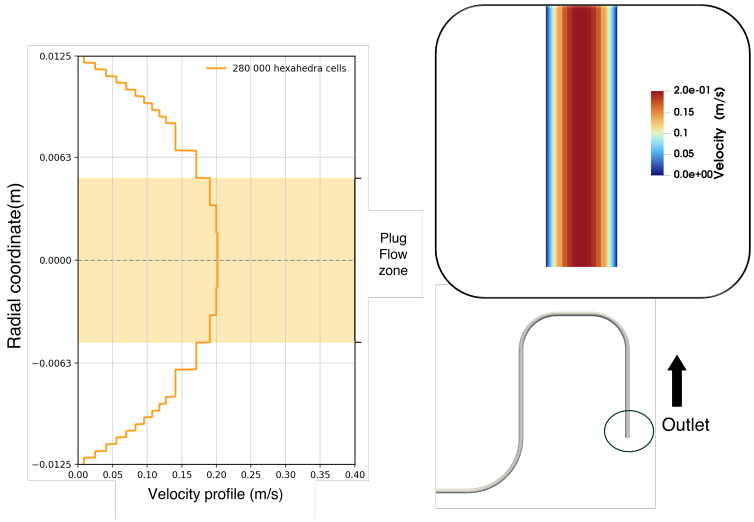


Figure 10. Velocity profile at the outlet

5.3. Validation

The numerical model was validated against physical printing trials by comparing volumetric flow rate, since local velocity cannot be measured directly within a closed pipe. For each trial, mix FIN 10 was prepared to a consistent flow table spread of approximately 16 cm, primed through the pump to eliminate air pockets, and extruded under conditions matching the simulation; the extruded volume was measured over a fixed time to obtain the flow rate, with each trial repeated for reliability.

The simulation predicted a volumetric flow rate of 3.26 L/min, obtained by integrating the analytical velocity profile over the pipe cross-section of the 280,000-cell mesh. For each trial, the deviation was calculated as the relative difference between the experimental and simulated flow rates, $(Q_{\text{experimental}} - Q_{\text{simulation}})/Q_{\text{simulation}} \times 100\%$ and the reported average deviation is the arithmetic mean of these nine individual percentage deviations.

Across nine physical trials, the measured flow rate averaged 3.98 L/min, corresponding to an average deviation of 22% (Table 7), ranging from 7% (Test 9) to 52% (Test 5). This scatter is attributed mainly to batch-to-batch variability in the rheological properties of the mix, likely driven by fluctuations in the moisture content and morphology of the recycled fine aggregates, together with minor pump pressure instabilities.

The relatively wide scatter observed here is broadly consistent with the literature on pumping-based validation of cementitious 3D printing materials. Analytical and numerical predictions of pumping pressure in 3D concrete printing have been reported to reach a maximum error of 13% at the lowest discharge rate tested, with the deviation increasing as the flow rate decreases [31], a trend broadly mirrored in the present results (Table 7). This scatter is further compounded by the recycled nature of the mix: recycled-aggregate concretes are documented to exhibit markedly higher heterogeneity in rheological measurements than their natural-aggregate counterparts [32], and the yield stress and plastic viscosity of 3D-printable mortars are known to evolve measurably during

the time elapsed between mixing and extrusion [33], introducing a further source of batch-to-batch variability beyond aggregate moisture content alone.

Table 7. Comparison between experimental and simulated volumetric flow rates

Test No.	Experimental flow rate (L/min)	Deviation from simulation
Test 1	3.60	10%
Test 2	3.80	17%
Test 3	4.20	29%
Test 4	4.00	23%
Test 5	4.95	52%
Test 6	3.80	17%
Test 7	4.00	23%
Test 8	4.00	23%
Test 9	3.50	7%
Average	3.98	22%

Part of the observed deviation may also reflect variability inherent to the experimental measurement itself rather than the numerical model. Volumetric flow rate in 3D concrete printing is typically obtained indirectly, from the extruded mass or volume collected over a fixed time, a process in which extrusion efficiency has been shown to vary measurably with process parameters even under nominally constant pump settings [34]; the reported deviations should therefore be interpreted as an upper-bound estimate of the true model error, since some portion is attributable to the experimental measurement chain rather than the CFD model itself.

In conclusion, the experimental validation indicates that the numerical model achieves a level of predictive accuracy broadly consistent with that reported elsewhere for pumping-based validation of printable and recycled-aggregate cementitious materials. The average deviation of 22%, while higher than typically reported for idealised laboratory flow tests such as slump or L-box trials, is considered acceptable given the combined effects of recycled-aggregate rheological variability, time-dependent material behaviour, and the inherent uncertainty of indirect flow rate measurement discussed above.

6. FEM simulation of post-extrusion structural behaviour

The preceding experimental and numerical work successfully verified the pumpability and extrudability of mix FIN 10 through trial printing, while the CFD simulation further characterised the velocity profile of the material as it was transported through the delivery pipe. However, the buildability and structural behaviour of the printed component, printed to 10 layers in the laboratory trial, remain unassessed. To gain a deeper and more explicit understanding of the structural behaviour of this recycled-material 3D-printed mortar, an FEM simulation was carried out using CalculiX.

6.1. Numerical setup

The post-extrusion structural response of mix FIN 10 was simulated in CalculiX, an open-source implicit finite element solver, using the Mohr–Coulomb failure criterion to capture the elastoplastic behaviour of the fresh mortar. All the necessary parameters were measured experimentally and are summarised in Table 5.

The reference geometry was a hollow rectangular wall (0.35 m $\times$ 0.17 m in plan, 0.045 m filament width), matching the trial-printed specimen. The geometry was discretised in SALOME into a fully hexahedral mesh of 8-node linear elements (C3D8), grouped into layer-wise element sets, a structure

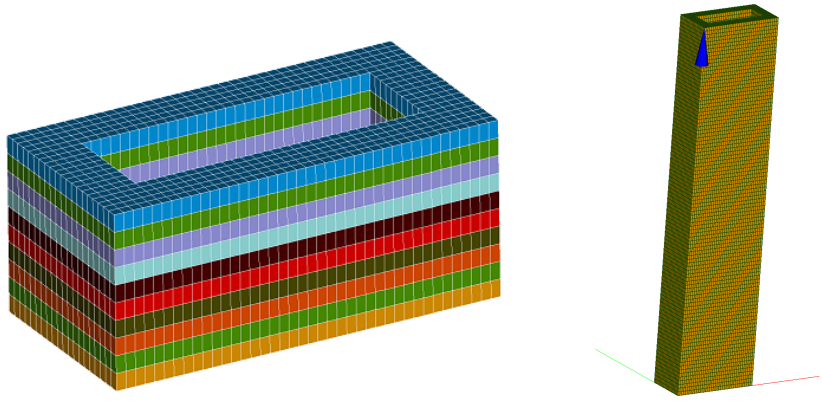
that lends itself naturally to reproducing the printing process step by step. The wall base was fully fixed, with all three translational degrees of freedom constrained, to represent the rigid printing bed.

Geometric nonlinearity was accounted for throughout the simulation (NLGEOM option in CalculiX), given the large deformations expected during progressive layer stacking and collapse. The layer-wise element sets were exploited through the MODEL CHANGE technique in CalculiX, which allows elements to be activated sequentially as printing progresses, closely mirroring the additive, layer-by-layer nature of the actual process: all layers except the base layer were initially removed from the model, and subsequent layers were incrementally reactivated one at a time, with the self-weight of all currently active layers reapplied at each step.

The buildability limit was identified as the layer at which the static analysis failed to reach numerical convergence, interpreted as the onset of structural collapse under self-weight. Since no dedicated eigenvalue buckling analysis was performed, the buckling nature of the observed failure mode, characterised by localised circular dimpling on the two long faces, was inferred from the deformation pattern obtained at the last converged increment prior to divergence, consistent with higher-order buckling behaviour associated with the greater slenderness of the wall's long faces.

Two meshes were established for this modelling programme. The first was a simple 10-layer mesh, used to investigate the structural behaviour of the specimen actually printed in the laboratory trial. The second was a 100-layer mesh, identical in cross-sectional geometry and layer dimensions to the first but grouped into 100 individual layer sets; the purpose of this extended mesh was to determine the buildability limit of the mix.

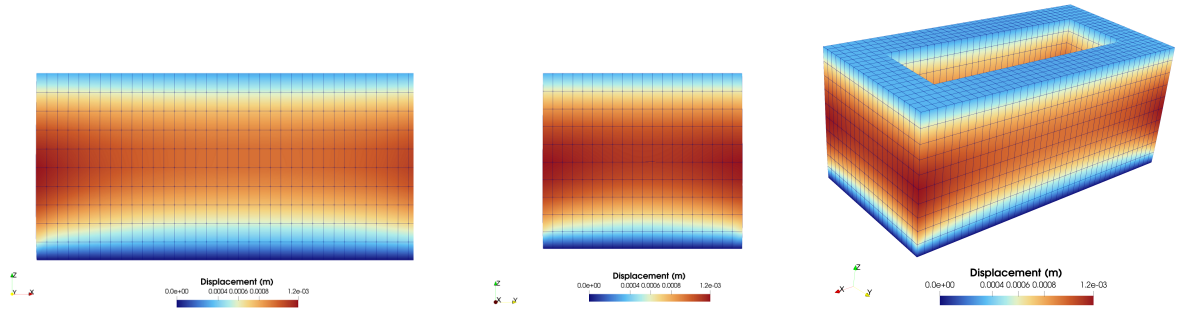
For both meshes, the algorithm reproduces the printing process step by step. The simulation begins with only the first layer active, resting on the fully fixed base, to which gravity is applied on its own. In each subsequent step, the next layer is reactivated and added to the model, and self-weight is reapplied to the entire stack of currently active layers, not just the newly added one, since a layer that was previously inactive does not retain memory of the load it carried before. This process is repeated layer by layer: for the 10-layer mesh, until all 10 layers are active, reproducing the actual printed specimen; for the 100-layer mesh, the same procedure continues until the solver can no longer find an equilibrium solution for the applied load, at which point the corresponding layer count is taken as the numerically predicted buildability limit.



(a) 10-layer mesh (b) 100-layer mesh

Figure 11. SALOME mesh of the printed wall: (a) 10-layer mesh, and (b) 100-layer mesh, both grouped into individual layer-wise element sets for sequential activation

6.2. Simulation results



(a) The front face (b) The side face (c) The isometric view

Figure 12. Displacement magnitude (U Magnitude, m) of the printed wall at layer 10, shown from the front face (a), side face (b), and isometric view (c)

The simulation results for displacement are presented in Fig. 12. The displacement field shows a pattern distinct from the stress distribution: since the base is fully fixed, displacement there is necessarily zero despite carrying the highest stress, while displacement accumulates with height as the material compresses under its own weight. The maximum displacement, however, does not occur at the top of the wall but in the mid-to-upper region, visible in views (a) and (b), reflecting a slight outward bulge under the combined effect of vertical compression and internal friction, most pronounced where the accumulated load remains substantial but the influence of the fixed base has diminished. This maximum displacement, on the order of 1.2×10^{-3} m, is small enough to be essentially imperceptible, consistent with the successful, deformation-free printing of the 10-layer specimen observed experimentally.

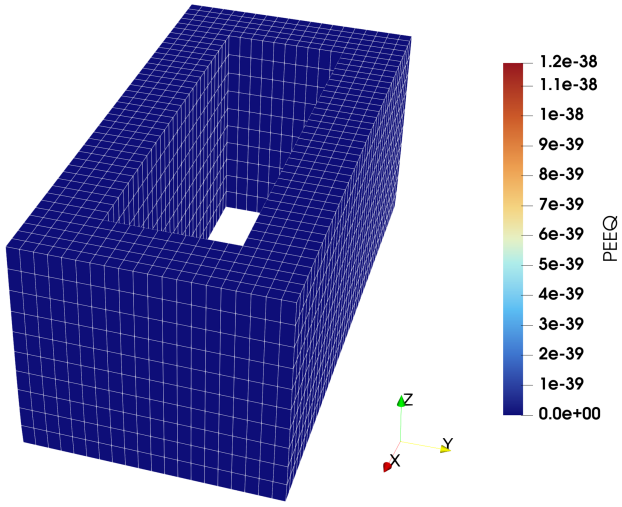
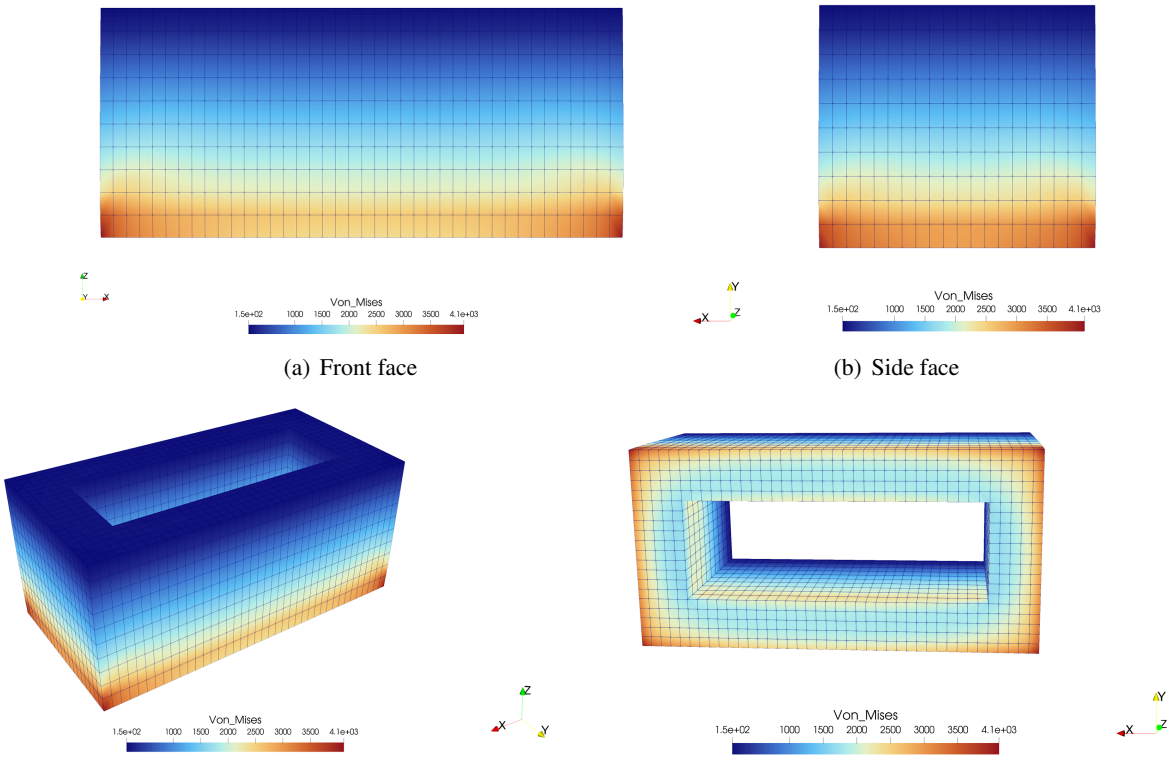


Figure 13. Equivalent plastic strain (PEEQ) contours at layer 10

The equivalent plastic strain (PEEQ) is also examined to check whether the mix has begun to yield anywhere in the component. As shown in Fig. 13, PEEQ remains effectively zero throughout the wall, of the order of 10^{-38}, several orders of magnitude below any physically meaningful strain. This confirms that the material stays entirely within the elastic regime at 10 layers: the stresses generated

by self-weight, although highest at the base, do not approach the mix's shear capacity, and the small displacements reported above are recoverable elastic deformation rather than permanent plastic flow.

The corresponding stress distribution is presented in Fig. 14, showing the front view (a), side view (b), isometric view (c), and plan view (d) of the printed wall. Von Mises stress peaks at the base of the wall, at approximately 4100 Pa, and decreases with height as the self-weight carried at each level diminishes, with the short faces (b, d) carrying a slightly higher stress than the long faces.



(a) Front face (b) Side face

(c) Isometric view (d) Plan view

Figure 14. Von Mises stress (Von_Mises, Pa) contours of the printed wall at layer 10: front face (a), side face (b), isometric view (c), and plan view (d)

This is consistent with the actual printing trial, in which the 10-layer specimen was printed successfully without any signs of instability or deformation large enough to compromise its geometry, indicating that the FEM model and the underlying material parameters are consistent with the observed structural behaviour of mix FIN 10 at this scale.

The 100-layer simulation was subsequently carried out after the structural behaviour of the 10-layer specimen had been established. Fig. 15 shows the maximum deformation of the printed component at the maximum height, corresponding to the point at which mix FIN 10 collapses. The results show that the wall successfully sustains its own weight up to a height of 540 mm, corresponding to the completion of 36 fully printed layers, with collapse occurring during the deposition of layer 37, corresponding to a numerically predicted buildability limit of 555 mm.

The most striking feature is the location and shape of the peak displacement. Rather than occurring at the base, where the wall is fully restrained, or at the top, where the most recently deposited material has carried the least accumulated load, the largest displacement, approximately 7.0×10^{-2} m, is concentrated in a single, well-defined, roughly circular dimple on the long face, positioned at ap-

proximately one-third to one-half of the total wall height, visible in Fig. 15(a).

This compact, concentric contour pattern is markedly more localised than the broad buckling band observed at the shorter critical height examined at earlier stages of this model's development, indicating a localised, higher-order buckling mode consistent with the substantially greater slenderness of the taller wall.

Both long faces of the wall dimple in the same way, mirrored on either side, which is consistent with a physical structural response rather than a numerical artefact. Away from the dimple, the base and top of the wall show almost no displacement, and the displacement increases sharply within just a few layers. This shows that the failure is sudden and localised, not a gradual sagging of the whole wall.

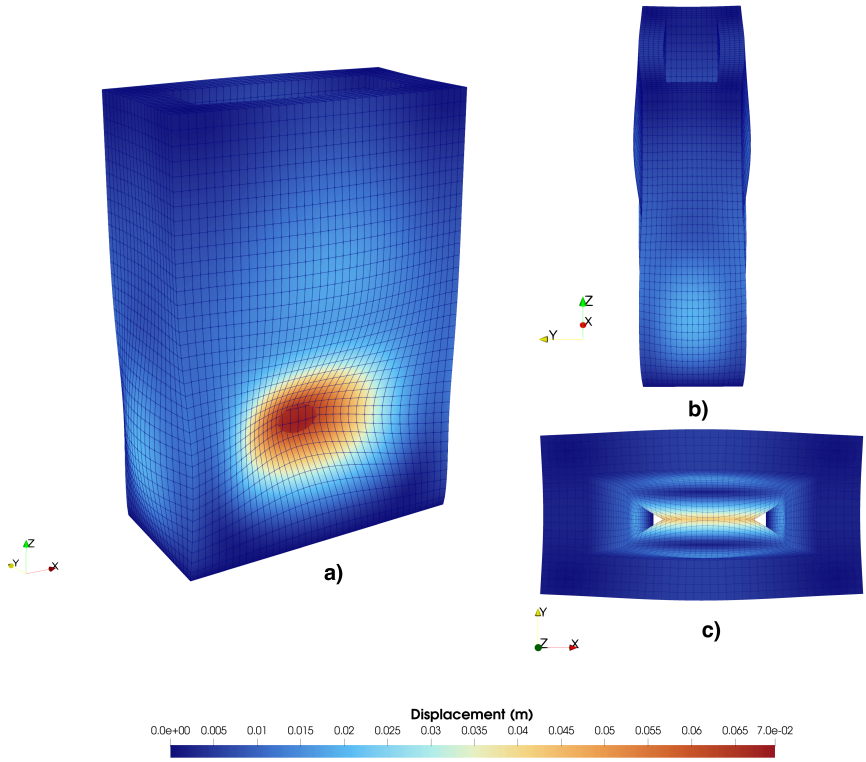


Figure 15. Displacement magnitude (U, m) at the critical 37-layer height: isometric view (a), front view (b), and plan view (c)

Fig. 15(c), the plan view taken at the critical height, confirms that this dimple does not extend across the full length of the long face: displacement is concentrated in a narrow, waisted region toward the centre, tapering off toward the short end walls, which remain close to undeformed. This is consistent with plate-buckling theory, where slenderness governs the critical buckling stress: for a given wall thickness, the long faces are inherently more slender than the short faces and therefore reach their critical buckling stress at a lower load, even though both faces carry a broadly similar average compressive stress. The short end walls, by contrast, show almost no displacement at all, behaving as stiff restraints for the adjoining long faces owing to their much greater local bending and torsional stiffness; deformation therefore concentrates toward the centre of each long face rather than distributing evenly along its length.

Fig. 15(b), the front elevation, shows comparatively little displacement across most of the wall's height, with only a slight, localised lightening in shade at the height corresponding to the dimple, consistent with this view capturing an edge-on projection of the same localised feature visible in (a).

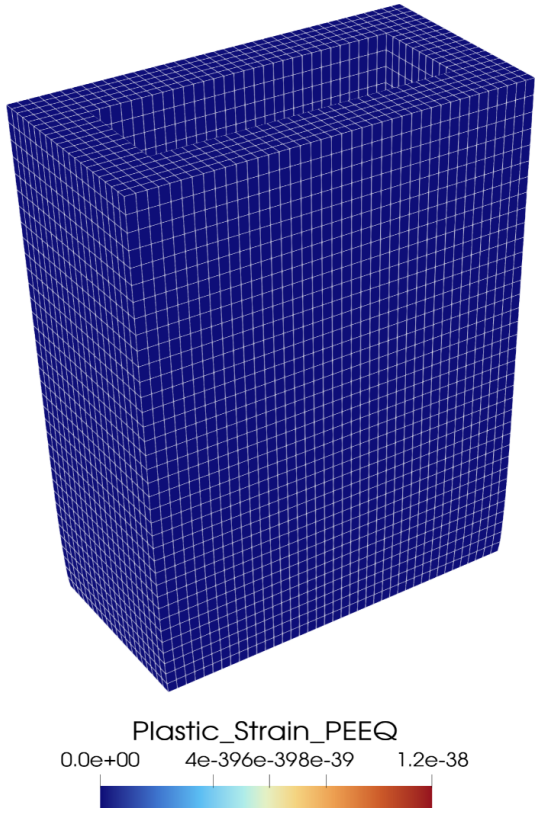


Figure 16. Equivalent plastic strain (PEEQ) contours at the critical 37-layer height

The equivalent plastic strain (PEEQ) field at the critical height (Fig. 16) remained at numerically negligible levels (on the order of 10^{-38}) throughout the entire structure, indicating that the material had not reached its Mohr–Coulomb yield surface anywhere in the wall at the point of collapse, a result consistent with elastic buckling, rather than plastic yielding, as the governing failure mechanism.

7. Discussions

The central finding, that mix FIN 10 collapses through elastic buckling rather than material yielding, is well supported by the broader FEM literature. Suiker's analytical elastic-buckling model predicts that thinner filaments reach their buckling limit at proportionally lower heights [18]; the comparatively narrow 45 mm bead width used here places the component well within the slenderness range where buckling, rather than plastic collapse, is expected to govern. This competition between plastic yielding and geometric buckling instability, producing the same asymmetric, localised bulging observed here, has also been reported using lattice and finite-element models by other researchers [17].

This observation is corroborated by recent parametric studies. Kocaer & Kul [35] found that reducing wall slenderness substantially increased the maximum printable height, identifying plan aspect ratio as the dominant design parameter, while [36] showed that replacing sharp corners with fillets or circular cross-sections improves buildability by redistributing stress away from the flat, unsupported wall faces where buckling initiates. This is consistent with the present results, where the four corners remained almost undeformed while the long, flat faces bulged outward and triggered collapse.

Taken together, these comparisons suggest that the buildability of mix FIN 10 is not solely a material limitation: redesigning the cross-section, for example through a thicker bead width or rounded corners, would be expected to increase the achievable printing height without requiring any change to the mix design itself.

The sequential linking of CFD and FEM within a single, experimentally calibrated framework also carries broader significance beyond the specific buildability limit identified here. Prior work on recycled-material 3D-printable mixes has generally reported flow behaviour, printability, or structural buildability as isolated outcomes, evaluated through separate experimental campaigns or disconnected numerical tools [13, 36]. By contrast, the present framework demonstrates that a single set of experimentally measured rheological and mechanical parameters can drive both the pumping-stage and post-deposition-stage predictions, offering a more complete, process-scale representation of how a recycled-material mix behaves from the moment it leaves the mixer to the point at which the printed structure may fail. While demonstrated here for a single mix and wall geometry, the sequential linking of CFD and FEM within one experimentally calibrated framework illustrates a methodology that could, in principle, be extended to other recycled-material formulations and structural configurations, offering a potential route to predicting both pumping behaviour and structural limits computationally rather than relying solely on trial-and-error printing. Confirming this generality, however, would require applying the framework to additional mixes and geometries, as noted in the Limitations and Future work sections.

8. Conclusions

This study developed and validated a sequential CFD-FEM computational framework to predict the behaviour of a 3D-printable mortar incorporating recycled sand and 10% RCCF as a partial cement substitute, from the pumping stage through post-deposition structural collapse. The following conclusions can be drawn:

1. Mix FIN 10 demonstrated satisfactory pumpability, extrudability, and buildability through trial printing on an actual 3D printer, confirming the technical feasibility of RCCF, an ultra-fine recycling by-product, as a partial cement substitute in 3D-printable mortar.

2. The CFD simulation of pumping flow, based on a Bingham representation of the measured rheological parameters, achieved an average deviation of 22% in volumetric flow rate against nine physical printing trials, a level of agreement considered satisfactory given the inherent sensitivity of fresh, recycled-material mortar to batch-to-batch variability.

3. The FEM simulation, using Mohr–Coulomb parameters obtained from fresh-state compression and direct shear testing, correctly reproduced the deformation-free behaviour of the 10-layer specimen printed experimentally, and identified a numerically predicted buildability limit of 555 mm (layer 37), with the wall successfully sustaining self-weight up to 540 mm (36 fully printed layers) before collapse initiated during deposition of the 37th layer.

4. The governing failure mechanism was identified as elastic buckling of the wall's long faces rather than plastic material yielding, a mode strongly influenced by the geometry of the printed cross-section and consistent with the broader buildability literature.

5. By sequentially linking both stages within a single, experimentally calibrated framework, this study demonstrates a process-scale computational methodology not previously applied to a 3D-printable mix incorporating recycled fine aggregate and recycled concrete fines, representing the principal novelty of this work.

Acknowledgment

The authors are grateful to Wallonia-Brussels International for providing financial support for the PhD thesis grant as part of the WalCoDeViet II project, entitled "Recycled Materials: Establishment and Training of Stakeholders in the Construction and Demolition Waste Recovery Sector in Vietnam" (2025–2027).

Declaration of generative AI and AI-assisted technologies

The author(s) declare that no generative AI or AI-assisted technologies were used in the preparation of this manuscript.

References

[1] Wang, X., Li, W., Guo, Y., Kashani, A., Wang, K., Ferrara, L., Agudelo, I. (2024). Concrete 3D printing technology for sustainable construction: A review on raw material, concrete type and performance. *Developments in the Built Environment*, 17:100378.

[2] Timm, K., de Villiers, W., van Zijl, G. (2026). 3D concrete printing in the waste hierachy: Reduce, reuse and recycle. *Circular Economy and Sustainability*, 6(2):110.

[3] Patil, Y. R., Dakwale, V. A., Ralegaonkar, R. V. (2024). Recycling construction and demolition waste in the sector of construction. *Advances in Civil Engineering*, 2024(1):6234010.

[4] Zhuang, Z., Xu, F., Ye, J., Hu, N., Jiang, L., Weng, Y. (2024). A comprehensive review of sustainable materials and toolpath optimization in 3D concrete printing. *npj Materials Sustainability*, 2(1):12.

[5] Xiong, B., Nie, P., Liu, H., Li, X., Li, Z., Jin, W., Cheng, X., Zheng, G., Wang, L. (2024). Optimization of fiber reinforced lightweight rubber concrete mix design for 3D printing. *Journal of Building Engineering*, 88:109105.

[6] Maroszek, M., Rudziewicz, M., Hebda, M. (2025). Recycled components in 3D concrete printing mixes: A review. *Materials*, 18(19):4517.

[7] Cuong, T. V., Kawamoto, K., Nga, T. T. V., Giang, N. H. (2023). Mechanical properties of synthetic aggregate pelletized by waste concrete fines in Vietnam. *Journal of Science and Technology in Civil Engineering (STCE) - HUCE*, 17(2):1–8.

[8] Quang, N. T., Cuong, T. V., Tan, N. N., Tan, N. H., Kawamoto, K., Giang, N. H. (2022). Experimental studies on behaviors of reinforced concrete column structures made of recycled aggregates under concentric loads. *Journal of Science and Technology in Civil Engineering (JSTCE) - HUCE*, 16(2):1–11.

[9] Bamigboye, G. (2026). Exploring the potential of *Senilia senilis* shells as a partial replacement for fine aggregate in hollow concrete block production. *Journal of Science and Technology in Civil Engineering (JSTCE) - HUCE*, 20(2S):55–64.

[10] Huong, N. L., Khanh, B. X., Nga, T. T. V., Dung, N. T. (2023). Crushed construction and demolition waste as reactive media in permeable reactive barriers to immobilize Pb(II) and Cd(II) from landfill leachate. *Journal of Science and Technology in Civil Engineering (STCE) - HUCE*, 17(2):145–153.

[11] Yuan, P., Wang, X., Huang, J., Shi, Q., Hua, M. (2026). Feasibility, mechanical properties, and environmental impact of 3D-printed mortar incorporating recycled fine aggregates from decoration and renovation waste. *Materials*, 19(8):1618.

[12] Al Thib, R., Belayachi, N., Bouarroudj, M. E., Bulteel, D., Rémond, S. (2023). A methodology for designing 3D printable mortar based on recycled sand. *Materials and Structures*, 56(9):165.

[13] Cavalcante, T. C., Filho, R. D. T., Reales, O. A. M. (2025). Rheological and environmental implications of recycled concrete powder as filler in concrete 3D printing. *Buildings*, 15(8):1280.

[14] Qian, H., Hua, S., Yue, H., Feng, G., Qian, L., Jiang, W., Zhang, L. (2022). Utilization of recycled construction powder in 3D concrete printable materials through particle packing optimization. *Journal of Building Engineering*, 61:105236.

[15] Comminal, R., Leal da Silva, W. R., Andersen, T. J., Stang, H., Spangenberg, J. (2020). Modelling of 3D concrete printing based on computational fluid dynamics. *Cement and Concrete Research*, 138:106256.

[16] Spangenberg, J., Leal da Silva, W. R., Mollah, M. T., Comminal, R., Juul Andersen, T., Stang, H. (2022). Integrating reinforcement with 3D concrete printing: Experiments and numerical modelling. In *Third RILEM International Conference on Concrete and Digital Fabrication*, 379–384.

[17] Rizzieri, G., Cremonesi, M., Ferrara, L. (2024). *Challenging the limits of fluid FEM modelling in 3D concrete printing*. Springer Nature Switzerland, 482–489.
[18] Vantyghem, G., Ooms, T., Corte, W. D. (2020). FEM modelling techniques for simulation of 3D concrete printing. *arXiv*.
[19] De Vlieger, J., Boehme, L., Blaakmeer, J., Li, J. (2023). Buildability assessment of mortar with fine recycled aggregates for 3D printing. *Construction and Building Materials*, 367:130313.
[20] Rehman, A. U., Kim, J.-H. (2021). 3D concrete printing: A systematic review of rheology, mix designs, mechanical, microstructural, and durability characteristics. *Materials*, 14(14):3800.
[21] Gerges, I., Abi Farraj, F., Youssef, N., Antczak, E., Hage Chehade, F. (2025). Methodologies to design optimum 3D printable mortar mix: A review. *Buildings*, 15(14):2497.
[22] Chen, S., Zhang, J., Yang, H. (2025). Effects of water-to-cement and sand-to-binder ratio on mechanical and drying shrinkage properties of low-carbon mortar containing biochar aggregate. *Materials*, 18(12): 2750.
[23] Luo, J., Wang, Q., Wang, L., Fang, M. (2026). A review of the rheological properties of 3D-printed concrete: Raw materials, printing parameters, and evolution mechanisms. *Buildings*, 16(6):1264.
[24] Jayathilakage, R., Rajeev, P., Sanjayan, J. (2022). Rheometry for concrete 3D printing: A review and an experimental comparison. *Buildings*, 12(8):1190.
[25] Zhang, C., Nerella, V. N., Krishna, A., Wang, S., Zhang, Y., Mechtcherine, V., Banthia, N. (2021). Mix design concepts for 3D printable concrete: A review. *Cement and Concrete Composites*, 122:104155.
[26] Fasihi, A., Libre, N. A. (2024). Interaction between material and process parameters during 3D concrete extrusion process. *Structures*, 70:107678.
[27] Jayathilakage, R., Rajeev, P., Sanjayan, J. G. (2020). Yield stress criteria to assess the buildability of 3D concrete printing. *Construction and Building Materials*, 240:117989.
[28] Wolfs, R. J. M., Bos, F. P., Salet, T. A. M. (2018). Early age mechanical behaviour of 3D printed concrete: Numerical modelling and experimental testing. *Cement and Concrete Research*, 106:103–116.
[29] Linh, L. C., Tri, M. C. (2023). Evaluating the performance of the RANS turbulence models for simulating wave propagation over a submerged breakwater using OpenFOAM. *Journal of Science and Technology in Civil Engineering (JSTCE) - HUCE*, 17(1):79–93.
[30] Greenshields, C. (2018). *OpenFOAM v6 user guide*. Accessed on 1 September 2026.
[31] Foulki, R., El Mesoudy, M., Cherkaoui, K. (2025). Numerical and theoretical analysis of pumping and extrusion in 3D concrete printing. *The International Journal of Advanced Manufacturing Technology*, 141(3-4):1653–1675.
[32] Faleschini, F., Jiménez, C., Barra, M., Aponte, D., Vázquez, E., Pellegrino, C. (2014). Rheology of fresh concretes with recycled aggregates. *Construction and Building Materials*, 73:407–416.
[33] Lee, H., Seo, E.-A., Kim, W.-W., Moon, J.-H. (2021). Experimental study on time-dependent changes in rheological properties and flow rate of 3D concrete printing materials. *Materials*, 14(21):6278.
[34] Maroszek, M., Rudziewicz, M., Hutyra, A., Dziura, P., Hebda, M. (2024). Evaluation of 3D concrete printing extrusion efficiency. *Applied Sciences*, 14(24):11866.
[35] Kocaer, O., Kul, A. (2025). Parametric analysis of design and operational parameters in 3D concrete printing of wall elements. *Journal of Building Engineering*, 115:114494.
[36] Khan, S. A., Koç, M. (2023). Buildability analysis of 3D concrete printing process: A parametric study using design of experiment approach. *Processes*, 11(3):782.